Aspects of Gas Storage: Confined Geometry Effects on the High-Pressure Adsorption Behavior of Supercritical Fluids

Simon Eder[a], Patrick Guggenberger[b,c], Tatiana Priamushko[b], Freddy Kleitz[b], Matthias Thommes[a,*]

[a] Institute of Separation Science and Technology, Friedrich-Alexander-Universität Erlangen-Nürnberg, Egerlandstr. 3, 91058 Erlangen, Germany, simon.eder@fau.de, matthias.thommes@fau.de

[b] Department of - Functional Materials and Catalysis, Faculty of Chemistry, University of Vienna, Währinger Str. 42, 1090 Vienna, Austria

[c] Vienna Doctoral School in Chemistry (DoSChem), University of Vienna, Währinger Str. 42, 1090 Vienna, Austria

Corresponding Author

* Matthias Thommes, Institute of Separation Science and Technology, Friedrich-Alexander-Universität Erlangen-Nürnberg, Egerlandstr. 3, 91058 Erlangen, Germany, Telephone: +49 9131 8527440, Fax: +49 9131 8527441, matthias.thommes@fau.de

Abstract

During the last decades, major progress was made concerning the understanding of subcritical, low-pressure adsorption of fluids like nitrogen and argon at their boiling temperatures in nanoporous materials. It was here possible to understand how structural properties affect the shape of the adsorption isotherms. However, within the context of gas storage applications, supercritical high-pressure gas adsorption is important. A key feature is here that the experimentally determined surface excess adsorption isotherm may exhibit a characteristic maximum at a certain pressure. For a given temperature and adsorptive/adsorbent system, the surface excess maximum (and the corresponding adsorbed amount) is related to the storage capacity of the adsorbent. However, there is still a lack of understanding how key textural properties such as surface area and pore size affect details of the shape of supercritical high-pressure adsorption isotherms. In order to address these open questions, we have performed a systematic experimental study assessing the effect of pore size/structure on the supercritical adsorption isotherms of pure fluids such as C_2H_4, CO_2, SF_6 over a wider range of temperatures and pressures on a series of model materials exhibiting well-defined pore sizes, i.e., ordered micro- and mesoporous materials (e.g., NaY zeolite, KIT-6 silica, MCM-48 silica). A fundamental result of our experiments is a unique fluid-independent correlation between the pressure of the surface excess maximum p^{max} (at a given temperature) and the pore size (by taking into account the kinetic diameter of the fluid and the underlying effective attractive fluid-wall interaction).

Summarizing, our results suggest important structure-property relationships allowing one to determine, for given thermodynamic conditions, important information related to the optimal operating conditions for supercritical adsorption applications. The insights may also serve as a basis for optimizing and tailoring the properties of nanoporous adsorbent materials for gas storage applications.

1 Introduction

In the last decades, major progress has been made concerning the understanding of subcritical adsorption of fluids like argon and nitrogen at their atmospheric boiling temperatures in nanoporous materials. It was possible to gain a fundamental understanding of how structural properties (e.g., the pore size) affect the shape of the adsorption isotherms, leading to novel methodologies that are now commonly used for characterization. In contrast, there are still many open questions concerning a detailed understanding of the underlying adsorption mechanism of supercritical fluid adsorption, which however is crucial for gas storage applications. Within this context, there is huge interest in exploring high pressure hydrogen adsorption on novel material classes (e.g., MOFs) [1–3]. Another focus is the adsorption and storage of fluids such as methane and carbon dioxide including the sequestration of carbon dioxide in nanoporous gas reservoirs (which might be a key technology to reduce the anthropogenic carbon dioxide emissions).

Taking a look at the past, the field of high-pressure adsorption started to evolve in the early 20th century with the introduction of steel made instruments capable of withstanding gas under high pressure. In these early days, some of the first high pressure adsorption data were reported on charcoal and activated carbon using various gases up to a pressure of 400 bar [4,5]. However, high-pressure adsorption experiments introduce several complexities, both in terms of collecting isotherm data and interpreting the results [6–13], especially in close vicinity to the critical point [14]. Therefore, in the recent time effort was invested in interlaboratory adsorption exercises, performed with different adsorptive-adsorbent systems at various conditions (from subcritical to highly supercritical) [15–19]. Within this context we would like to highlight the very recent high-pressure carbon dioxide and methane reference adsorption data sets [15,16].

Beside the difficulties arising with the experiments, one of the main problems of high-pressure adsorption is the fact that one cannot directly experimentally determine the (absolute) adsorbed amount n^a directly. Instead the so-called surface excess amount n^σ [6] (first introduced by Gibbs [7]) or the more recently introduced net adsorption [8,9] can be determined by commonly used manometric and gravimetric measurements, where the majority of experimental high pressure adsorption data reported in the literature is still solely based on the surface excess.

The relation between the surface excess amount and the (absolute) adsorbed amount is given in the simplest case by the following relation:

$$n^\sigma = n^a - \rho_{Bulk}V^a \tag{1}$$

where ρ_{bulk} is the density of the bulk gas, whereby V^a represents the adsorption space, which is inherently determined by the underlying density profile of the adsorbate which is often not known [6]. The the absolute adsorption (n^a) may be defined as the amount of gas in the adsorbed layer (or the adsorption space V^a), i.e., the sum of the experimentally measured excess adsorption and the gas in the volume of the adsorbed phase, owing to the applied gas density.

For (many) subcritical conditions (e.g., argon and nitrogen adsorption at their atmospheric boiling temperature), n^a and n^σ are essentially identical due to the negligible bulk gas density compared to the adsorbate phase. Even up to pressures of about 10 bar, it could be shown that surface excess and adsorbed amount do not deviate much [20]. However, for higher pressures and at supercritical conditions it is typical that the bulk density reaches non-negligible values [6]. In this case, the conversion from surface excess to adsorbed amount is challenging because, as already mentioned, V^a is not known a priori. However for narrow pores, in particular for purely microporous materials, it has been shown that V^a can be approximated by the micropore volume [10,12]. Within this context various approaches were proposed to address the challenge of converting surface excess (obtained at supercritical conditions) into (absolute) adsorbed amount and a good overview can be found in ref. [11].

A particular feature of supercritical surface excess adsorption isotherms is that the isotherm exhibits a characteristic maximum associated with finite compressibility of the adsorbate phase, i.e., the fluid in the adsorption space, while the bulk gas phase can be further compressed with increasing density [21,22]. As the pressure is further increased, the density of the bulk gas phase approaches that of the adsorbate phase, leading to a decrease of the surface excess and, finally, the excess amount adsorbed should become zero. Within this context, it has been shown that the pressure at which the surface excess isotherm exhibits its maximum [11–13] is also a good indicator for the pressure region associated with the (absolute) adsorbed amount approaching its maximal value. Hence, determining the experimental condition associated with the surface excess maximum provides important information about the maximum gas adsorption capacity for a certain adsorbent.

However, there has been only limited work studying the effect of textural properties on surface excess adsorption. Grand-Canonical Monte-Carlo (GCMC) studies focusing on the supercritical adsorption of Lennard Jones fluids in carbon slit pores suggest that the pressure at which the surface excess isotherm exhibits its characteristic maximum and the shape of the isotherm depend on the pore diameter [23,24]. Further theoretical and experimental work was focusing on a better understanding of the supercritical adsorption mechanism [21,25–31]. Experiments using two mesoporous controlled pore glasses with nominal pore sizes of 7.5 and 35 nm showed that with decreasing pore size the surface excess maximum of CO_2 is indeed shifted towards lower pressures [30]. On silica aerogel (having a mode pore diameter of about 9 nm) also the surface excess adsorption behaviour of additional interesting supercritical fluids such as CH_4, C_2H_6, and C_3H_8 was investigated [31]. For purely microporous materials (such as MOF based materials), hydrogen uptake was found to correlate mainly with the apparent surface area and the micropore volume [32,33].

However, a clear and comprehensive understanding of how pore structure and the resulting confinement affect supercritical adsorption behavior over a wide range of pore sizes has not been achieved. Yet, this fundamental understanding is important to predict, as already mentioned, gas storage conditions (e.g., the operating pressure), to tailor novel nanoporous materials for gas storage applications or to develop energy-efficient adsorption-based separation processes for industrial applications.

The objective of this work is to start filling this gap by systematically investigating the fundamental mechanisms behind supercritical high-pressure adsorption. For this purpose, we utilized in contrast to the majority of previous works, a series of model materials with well-defined pore sizes, i.e., ordered micro- and mesoporous materials such as zeolites and mesoporous silica molecular sieves (e.g., KIT-6 silica). Those materials are characterized by argon ad- and desorption isotherms and dedicated state-of-the-art non-local density functional (NLDFT) methods. Furthermore, all the selected mesoporous molecular sieves have a similar surface chemistry, what is a basic requirement for a later systematic evaluation. High-resolution supercritical surface excess isotherms of C_2H_4, CO_2 and SF_6 at three different comparable temperatures are then determined. C_2H_4 was selected as model fluid, allowing to refer also to existing fundamental supercritical adsorption data on nonporous carbon materials [21], while a better understanding of the adsorption mechanism of the dangerous greenhouse gases CO_2 and SF_6 is of huge importance for optimizing corresponding gas storage applications [34–38].

Our systematic study contributes to a better understanding of the underlying adsorption mechanism of supercritical fluids in nanoporous materials. The data suggests for a given temperature a novel and unique correlation between the pressure of the surface excess maximum p^{max} and the mesopore size taking into account the kinetic diameter of the fluid and the attractive fluid-wall interaction for a given adsorptive/adsorbent system. The obtained structure-property relationships have the potential to guide in the selection of proper operational conditions in supercritical adsorption applications and may also contribute to the development of a optimized adsorbent materials tailored towards gas storage or separation applications

2 Materials & Methods

2.0 Materials (Adsorbents)

In this work, seven ordered micro- and mesoporous model materials are investigated: SBA-3 (2.5 nm), MCM-48 (3.3 nm) and three samples of KIT-6 with different pore sizes. These pure silica materials are associated with a well-defined cylindrical pore geometry and a narrow pore size distribution (PSD). Standard KIT-6, which can easily be synthesized in the range from 4 to 12 nm (by alteration of the hydrothermal treatment temperature) [39], and MCM-48 materials have a three-dimensional interconnected pore network [40,41], whereas SBA-3 has a pseudo one-dimensional pore geometry. Similar to classical MCM-41 silica, SBA-3 exhibits a highly ordered 2-D hexagonal mesostructure, but it is prepared under acidic conditions using a mixture of cetyltrimethylammonium bromide (CTAB), water, and HCl, with tetraethoxysilane (TEOS) as silicon precursor. SBA-3 is by far less studied than other mesoporous molecular sieves (e.g., MCM-41) however it represents a good model system in the lower mesopore range (~2 nm), and remains to be explored more in detail in terms of its adsorption behavior especially. Synthesis of all these materials was performed according to highly reproducible reported

protocols[41–43], the details of which can be found in the Supporting Information. FD121, referred here as CPG (18.5) and a member of the controlled porous glasses, was obtained from the Bundesanstalt für Materialforschung und -prüfung (Berlin, Germany) and a microporous NaY (1.1 nm) zeolite was obtained from the National Institute of Standards and Technology (Gaithersburg, USA).

2.1. Textural Characterization by Gas Adsorption

Textural characterization was performed by argon 87 K adsorption, which allows for accurate pore size an surface area assessment [44]. Prior to the adsorption experiments, the mesoporous silica materials were degassed at 150 °C for 12 h while the microporous NaY zeolite was outgassed at 550 °C for 12 h, both under turbomolecular pump vacuum. Isotherms were recorded in a relative pressure range of approximately 10^{-5} up to 1 for each material using a commercial volumetric sorption analyzer of type autosorb IQ (Model 7) by Anton Paar QuantaTec (former Quantachrome, Boynton Beach, USA). The skeletal density of each material is determined using a commercial pycnometer of type Ultrapyc1600e from Anton Paar QuantaTec (Boynton Beach, USA) and helium (298.15 K) as probe molecule.

2.2 High-Pressure Experiments

High-pressure measurements were performed using a Rubotherm (Bochum, Germany) magnetic suspension balance which has an accuracy of 10 **µg**. A detailed description of the functionality of such instruments is given elsewhere [45].

The gas dosing unit, which can be heated up to 80 °C in order to prevent condensation, is self-built. Since a PID-controller caused pressure fluctuations in close vicinity to the critical point, the temperature of the condensation-protection was controlled by a manual current control. The piping is insulated with a 1 cm thick layer of fiberglass wool to prevent short-term fluctuations in the airflow of the fume hood from causing temperature changes in the piping. The standard 10 and 500 bar pressure transducers of type PMP4000 from Druck Incorporated (New Fairfield, USA), are complemented by a digital highly accurate 150 bar pressure transducer of type Adroit6200 from Druck Incorporated, which has a certified accuracy of +/- 0.04 % of the maximum pressure reading in the temperature range of -40 to +80 °C. The analog signal was converted without loss of information due to discretization using the 12-bit analog-to-digital converter of a Labjack-U3 manufactured by the LabJack Corporation (Lakewood, USA). A 4-wire platinum PT-100 electrical resistance thermometer calibrated with a reference thermometer from WIKA (Klingenberg am Main, Germany) was used to measure the temperature inside the instrument. The temperature was controlled by a heat transfer fluid and an advantageous serial-up configuration [14] was chosen. The thermostat used was a Proline RP845 manufactured from LAUDA (Lauda-Koenigshofen, Germany), which has a temperature stability of +/- 0.1 K. Gas was supplied either directly from a gas bottle or from a syringe pump of type 260D from Teledyne Isco (Lincoln, USA).

Turning towards data processing of the experimental setup, the underlying procedure to convert gravimetric measurement data into surface excess isotherms is given in the literature [14,46]. With

regard to the buoyancy correction, we used the so-called theoretical and blank-corrected approach [46], i.e., the buoyancy force is calculated theoretically and deviations in the calculation are corrected by blank isotherms. Three independent blank isotherms were recorded for each gas and temperature. Hence, for each temperature the blank correction was based on an averaged data set obtained from the corresponding runs (see Supporting Information Table S1). The measurement profile (i.e., the number of isotherm points, the measurement length per isotherm point) is the same as for the later experiments. The accuracy of the adsorption setup and the applied experimental procedure was checked by utilizing the NIST standard material RM8850 (NaY (1.1)) and comparing the adsorption data of CH_4 on the latter one with the corresponding reference data (see Supporting Information Figure S2).

2.3 Adsorptives

In the scope of this work, three gases were used. The critical parameters and kinetic diameters of all gases are given in Table 1. The first series of measurements was conducted using ethylene (>99.995 %). Experiments were performed at a temperature of 15.00, 20.00 and 25.00 °C, corresponding in terms of reduced units to $\mathbf{T_{red}}$ (T/ T_{crit}) of 1.021, 1.038 and 1.056. The second used fluid was carbon dioxide (>99.9995 %). Experiments were conducted at 38.00, 43.15 and 48.20 °C (corresponding in reduced terms to $\mathbf{T_{red} = 1.023, 1.040, 1.057}$) which enables a direct comparison to the ethen sorption data. For the last fluid, SF6, adsorption isotherms were performed solely at ($\mathbf{T_{red} = 1.023}$) (due to its massive global warming potential), allowing a direct comparison with C_2H_4 and CO_2. Beside the temperature, all experimental data are given with regard to state variables in form of reduced units.

Table 1: Critical parameters and kinetic diameter of ethylene, carbon dioxide and sulfur hexafluoride

	Ethylene	Carbon Dioxide	Sulfur hexafluoride	Unit
T_c	282.30 (9.2 °C)	304.2 (=31.0 °C)	318.7 (= 45.6 °C)	K
p_c	50.4	73.8	37.5	bar
$\boldsymbol{\rho}_c$	214.2	467.6	742.3	kg m^{-3}
$\boldsymbol{\sigma}$	0.39	0.33	0.55	nm

3 Results and Discussion

3.1 Textural Characterization

High-resolution argon (87 K) ad- and desorption isotherms of the model materials are illustrated in Figure 1a. Classifying the isotherms with regard to the IUPAC technical report [44], all isotherms except the NaY zeolite exhibit a type IV shape. This kind of isotherm corresponds to mesoporous materials due to the presence of capillary condensation.

The isotherms obtained on KIT-6 and CPG silica show type IV(a) isotherms, revealing pronounced type H1 hysteresis, which can be attributed to delayed condensation [44,47,48] caused by a metastable pore fluid. Since with decreasing pore size, the relative pressure of capillary

condensation is shifted towards lower values, due to the increasing confinement of the fluid within the pore [47], the isotherms indicate that the materials have different pore diameters.

Turning towards the isotherms of MCM-48 (3.3) and SBA-3 (2.5), no hysteresis can be observed, i.e., both can be classified as type IV(b), which is characteristic for reversible capillary condensation/evaporation [44,48]. The argon (87 K) isotherm of NaY (1.1) can be classified as a type I(a) isotherm, which is typical for microporous materials ($d_{pore} <\sim 1$ nm) [44] with pronounced adsorbent-adsorptive interactions.
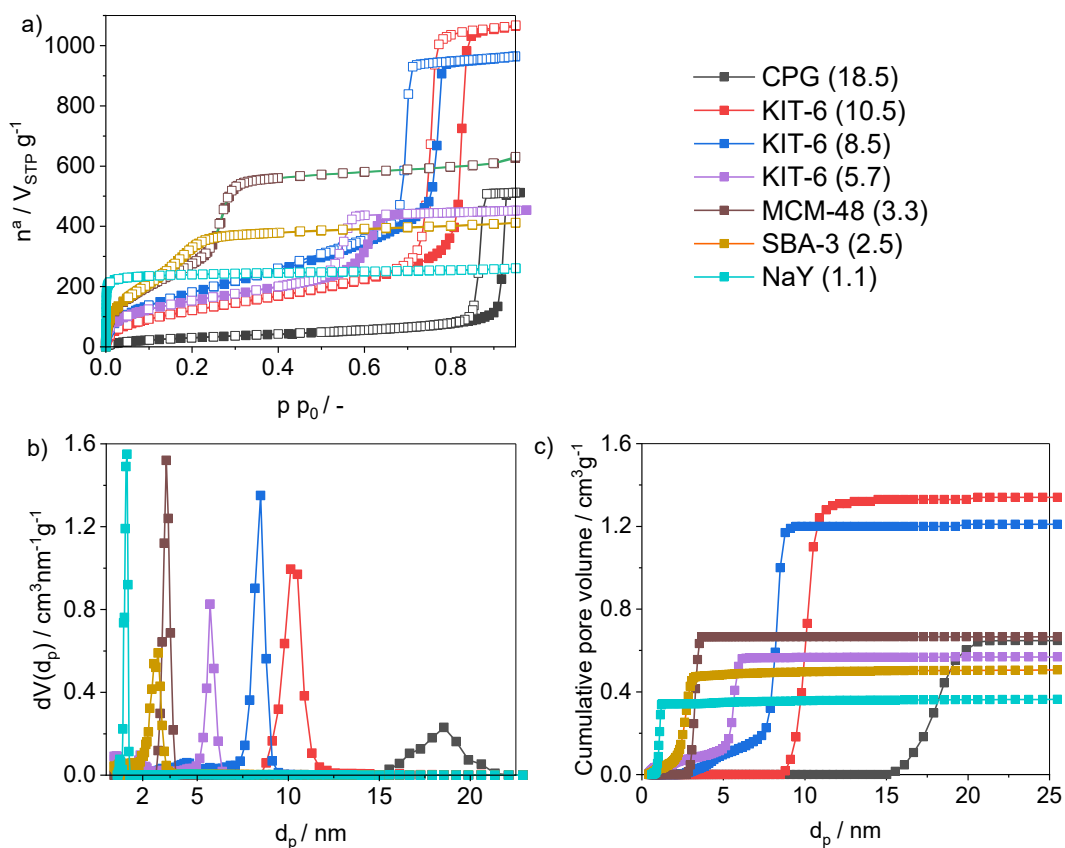
Figure 1: a) High-resolution argon (87 K) ad- and desorption isotherms. b) PSD and c) CPV of the ordered micro- and mesoporous model materials obtained by applying dedicated NLDFT kernels.

To obtain the pore size distribution (PSD) and the cumulative pore volume (CPV), dedicated NLDFT kernels were applied on the argon (87 K) isotherms. For all isotherms showing a type IV behavior, the equilibrium NLDFT kernel for argon adsorption in cylindrical silica pores at 87 K was applied on the desorption branch. Turning towards NaY (1.1), in order to account for the cage-like structure of the pores [49], a dedicated combinatorial NLDFT [50] method assuming spherical zeolite pores in the micropore region and cylindrical siliceous pores for diameters larger than 2 nm was used.

The PSDs of all materials, illustrated in Figure 1b, show very narrow PSDs ranging from 1.1 nm to 18.5 nm. This unique ensemble of well-defined micro- and mesoporous model materials allows the pressure at which the surface excess isotherm exhibits a maximum and the overall shape of the isotherm to be directly correlated to the pore size. Analyzing the CPV, given in

Figure 1c, all materials, except SBA-3 (2.5) and (obviously) NaY (1.1), do not exhibit a significant amount (>10 %) of microporosity.

Regarding the specific surface area of the samples, under certain carefully controlled conditions, the specific BET surface area of mesoporous materials can be considered as the probed accessible surface area [51]. Details of surface area assessment using the BET method can be found in the literature [48,52,53]. Since the formation of the first and second layer might not be distinguishable in very narrow pores (<2 nm), a straightforward application of the BET theory is limited to materials which do not contain microporosity [44,54], and only apparent surface areas can be obtained. By using argon as a probe molecule, an overestimation of the specific surface area due to the specific interactions between the quadrupole moment of nitrogen and polar surface sites is omitted (since in this case the cross-sectional area may be smaller than the customary value of 0.162 nm^2) [53,55]. For materials showing a well-defined type IV(a) isotherm, the specific surface area is obtained within the relative pressure range of 0.05 to 0.3. For MCM-48 (3.3), showing a type IV(b) isotherm, care is taken since pore filling is observed very close to the pressure range where monolayer-multilayer formation occurs [52]. Therefore, the theory is applied in a pressure range of 0.05 to 0.1. For materials showing a significant degree of microporosity, e.g., SBA-3 (2.5) and NaY (1.1), the apparent surface area is determined using the Rouquerol criteria [54].

Table 2: Mode pore diameter d_{pore} and specific surface area S of the utilized model materials.

Material	d_{pore} [nm]	S [m^{2}g^{-1}]
CPG (18.5)	18.5	106
KIT-6 (10.5)	10.5	418
KIT-6 (8.5)	8.5	628
KIT-6 (5.7)	5.7	493
MCM-48 (3.3)	3.3	862
SBA-3 (2.5)	2.5	1501
NaY (1.1)	1.1	843

3.1 High-Pressure Surface Excess

The high-pressure surface excess n^σ isotherms of ethylene at $T_{red} = 1.021$, carbon dioxide and sulfur hexafluoride at $T_{red} = 1.023$ are illustrated as a function of the pressure in Figure 2 (for the experimental data at $T_{red} = 1.038, 1.056$ see Supporting Information Figure S3 and S4). For low pressure (approximately below 10 bar), all surface excess isotherms show a steep initial rise. Following on the latter one, all surface excess isotherms exhibit a characteristic maximum at a pressure p^{max}. Considering the pressure where the isotherms show this characteristic feature, a shift of the latter one to lower values with decreasing pore size can be observed. Regarding the overall shape of the surface excess isotherms, with decreasing pore size the surface excess maximum becomes less pronounced, although all studied model materials exhibit well-defined pore structure with a comparable very narrow pore size distribution (PSD). Hence, the observed rounding of the surface excess isotherm, i.e., less well-defined surface excess maximum, is not caused by different widths of the PSDs of the materials. For the small micropores of the NaY

(1.1) zeolite, one may not observe a distinct maximum (for the given experimental conditions) at all.

Following the surface excess maximum, all isotherms show (at elevated pressures) a steep decrease of the surface excess isotherms with increasing pressure.
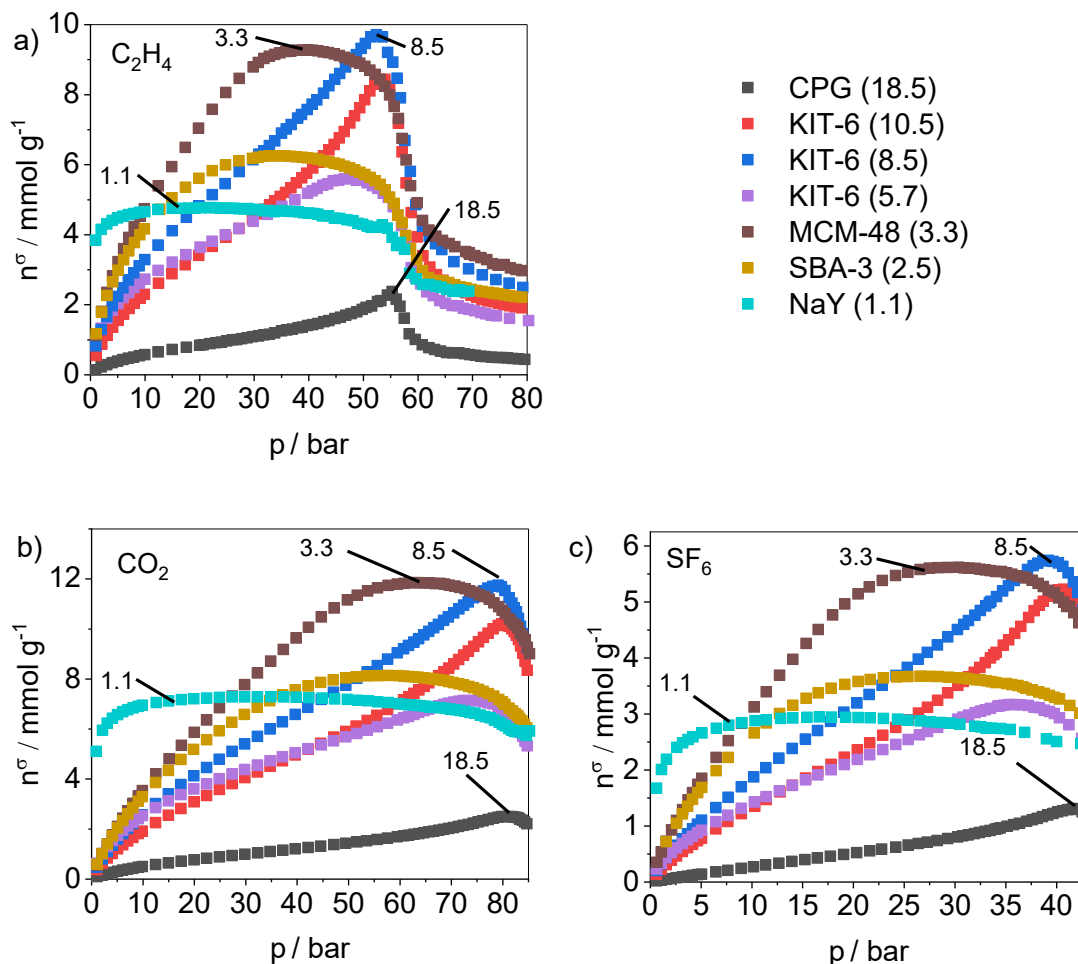
Figure 2: High-resolution surface excess isotherms of a) C_2H_4 at $T_{red} = 1.021$ b) CO_2 at $T_{red} = 1.023$ c) SF_6 at $T_{red} = 1.023$ obtained on the micro- and mesoporous model materials as a function of the system pressure.

While the data in Fig. 2 reveal that the pressure where the surface excess isotherms exhibit a maximum depends on the pore size, the maximal surface excess amount is not correlated with the specific pore volume (see Fig. 1c) for a given material. If however the surface excess is converted into the absolute (adsorbed) amount, the adsorption capacity is a function of the total pore volume. This is demonstrated in Fig. S1 for three samples exhibiting micro- and narrow mesopores, for which the approximation that V^{pore} equals V^a can be justified. Furthermore, the data in Fig. S1 confirm that the pressure of the surface excess maximum is a good indicator for the pressure region associated with a maximal value in the (absolute) adsorbed amount.

Prior to the further analysis, experimental data of all three gases are converted and illustrated as a function of the reduced pressure p_{red} $(= p\, p_{crit}^{-1})$ and the reduced density ρ_{red} $(= \rho\, \rho_{crit}^{-1})$, given in Figure 3.
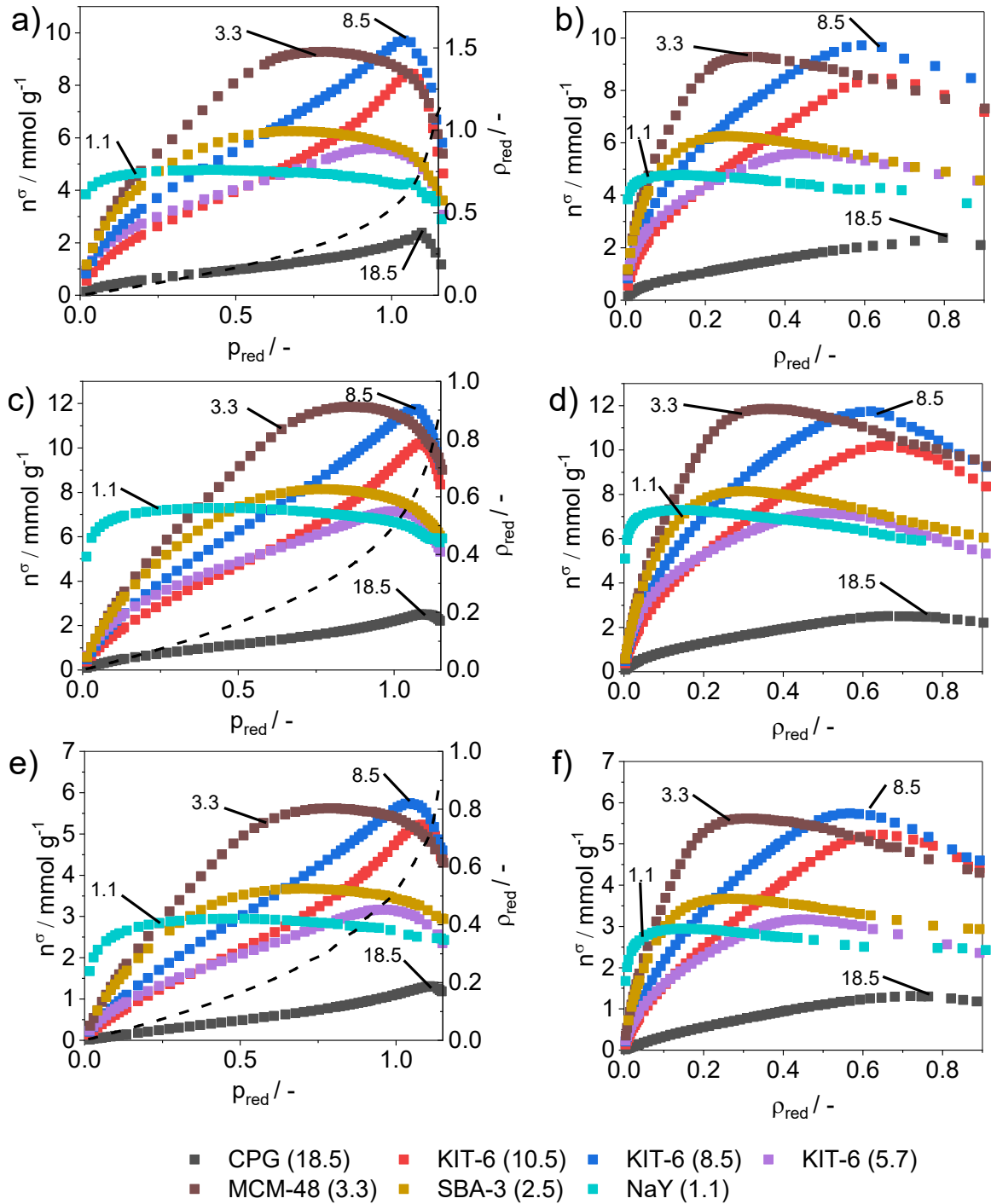
Figure 3: High-resolution surface excess isotherms of obtained on the micro- and mesoporous model materials for a) C_2H_4 at $T_{red} = 1.021$ as function of the reduced pressure, whereas the reduced bulk density is given as black dashed line and b) as a function of the reduced density c) CO_2 at $T_{red} = 1.023$ as function of the reduced pressure, whereas the reduced bulk density is given as black dashed line and d) as a function of the reduced density e) SF_6 at $T_{red} = 1.023$ as function of the reduced pressure, whereas the reduced bulk density is given as black dashed line and f) as a function of the reduced density.

Comparing the location of the surface excess maximum, for instance for the largest pores of CPG (18.5), p^{max} is here located above the critical pressure ($p_{red} = 1$) whereas if the data are

displayed as a function of the reduced density the surface excess maximum lies below the critical density (ρ_{red} = 1). This suggests that the position of the surface excess maximum is correlated with the compressibility of the bulk phase, which is shown in Figure S5 (in the Supporting Information). The maximal compressibility of the utilized fluids is for the given experimental studied temperature above the critical pressure, but below the critical density. However, with decreasing pore size the surface excess maximum shifts below bulk critical values for p^{max}, indicating that now in addition to the bulk fluid also the state of the pore fluid, which is affected by confinement, contributes to the position of the surface excess maximum.

Furthermore, Figure S5 in the Supporting Information clearly reveals that the bulk compressibility, similar to the surface excess isotherms exhibits a maximum and a cusp-like behavior, which becomes less pronounced and rounded with increasing temperature and distance to the critical temperature, i.e., the more supercritical the state of fluid is. The effect of bulk compressibility is also reflected in effect of temperature on the surface excess maximum $\boldsymbol{n^{\sigma}}$ which is s shown for C_2H_4 in KIT-6 silica of 8.5 nm as a function of reduced pressure $\mathbf{p_{red}}$ in Figure 4a and reduced density $\boldsymbol{\rho_{red}}$ in Figure 4b.

The data in Figure 4a reveal a distinct maximum which is shifted to higher pressures with increasing temperature but also reveals, as it has observed before [21,27,56], that the isotherm obtained at the lowest temperature intersects those at higher temperature. However, no such crossover occurs if the surface excess isotherms are plotted as a function of the bulk gas density. This different temperature behavior of the surface excess reflects the effect of the state of the bulk fluid [27]. This is also manifested in the observed temperature dependence of the surface excess maximum, which shifts with increasing temperature to higher reduced pressure whereas the overall course of the isotherm smooths out, i.e., an analogue behavior can be observed for the bulk compressibility (see Figure S5). In addition, here the maximum in the compressibility shifts to larger reduced pressures with increasing temperature and the compressibility maximum becomes less pronounced.
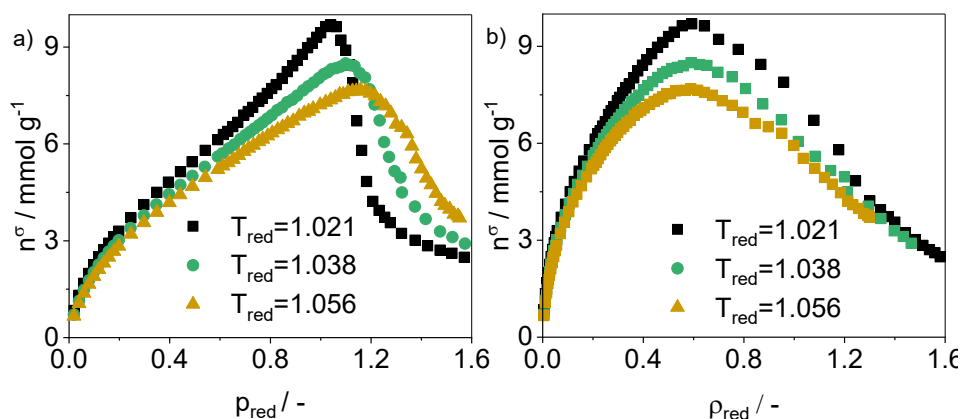
Figure 4: C_2H_4 surface excess isotherms obtained on KIT-6 (8.5) at various temperatures as a) function of the reduced pressure and b) function of the reduced density.

Effect of surface area and pore size

To better compare the surface excess adsorption behavior obtained on the different material particularly at lower pressure, where the surface excess/mass depends strongly on the specific surface area, it is desirable to display the surface excess amount in form of the surface excess concentration (i.e., $\Gamma = n^\sigma / S_{BET}$) as shown in Figure 5.

Based on high-resolution and accurate sorption data and the utilization of argon as probe molecule for obtaining reliable specific surface areas, it is possible (using exemplary C_2H_4 adsorption data) to here show excellent agreement between the surface excess isotherms for reduced pressures $\mathbf{p_{red}}$ below 0.25, evidencing that the surface area dominates this part of the isotherm, as recently suggested [30]. Furthermore, this observation indicates that the adsorption potential for all silica materials used in this work is indeed essentially identical and that the adsorption within the first layers is not significantly affected by the pore size for the studied mesoporous materials. However, for high pressures (starting at $p_{red} > 0.5$) the isotherms start to diverge. Since this behavior is not to be explained by the surface, this part of the isotherm must be dominated by the state of the fluid in the core of the pore volume, which depends on the pore size. The surface excess concentration is the highest for CPG (18.5), followed by KIT-6 (8.5), then by KIT-6 (5.8 nm) and finally MCM-48 (3.3). As shown in Figure 3, the surface excess concentration maxima are shifted to higher red. pressures with increasing pore size, while for the largest pore sizes cusp-like surface excess maximum can be observed, which become more and more less distinct with decreasing pore size. Based on the data shown in Figure 5, we propose to divide the supercritical surface excess isotherms into three regimes: while the first regime is entirely dominated by the surface area of the pore, the second regime reflects the effect of pore size on the state of pore fluids while the position of the surface excess maximum seems to be controlled by the interplay of the state of pore fluid with the bulk fluid state, while the third regime of the sharp decline of the surface excess is essentially for all pores entirely dominated by the properties of the bulk fluid. Classifying the C_2H_4 surface excess isotherm (at the temperatures studied) on NaY (1.1) into this picture, the broad plateau of the isotherm is reached at reduced pressures below 0.25, indicating that the surface excess isotherm of microporous materials is solely dominated by the surface and bulk mechanisms.
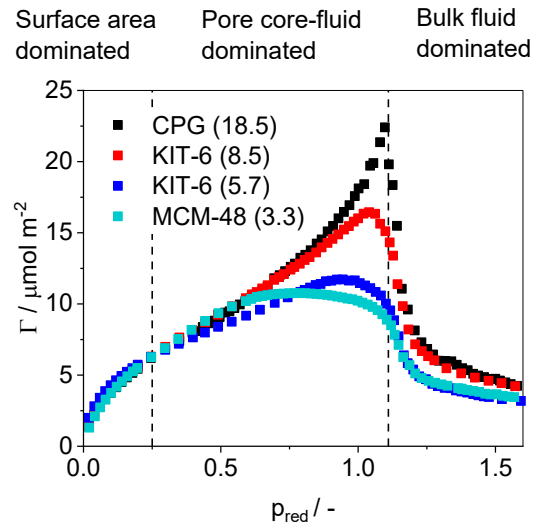
Figure 5: Surface excess isotherms normalized with regard to the specific surface area for a variety of mesoporous model materials at T_{red} = 1.021.

To have a closer look at the pore-size dependence, for each set of material and operation conditions, the reduced pressure at which the supercritical surface excess isotherm exhibits a maximum is extracted (by fitting a second degree polynomial to the data points around the maximum) and is illustrated as a function of the pore diameter in Figure 6. Within the diagram, the micro- and mesopore regions are divided by a vertical black dashed line. With increasing pore-size, the reduced pressure is asymptotically approaching an upper limit while the overall course is shifted to higher reduced pressures with increasing temperature. This indeed indicates that for the CPG sample with a pore diameter of about 18.5 nm at the investigated temperatures, the surface excess maximum is not anymore affected by the pore size.
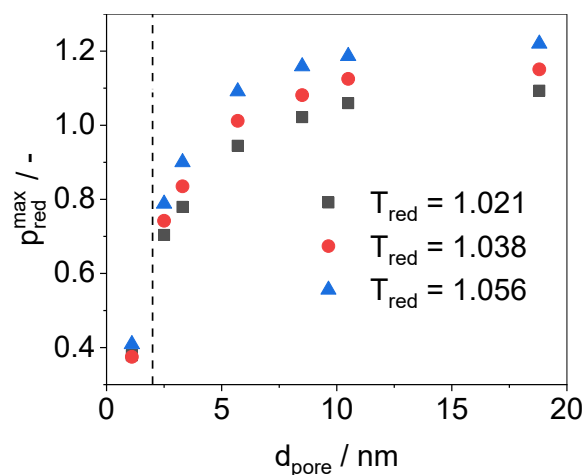
Figure 6: Reduced pressure where the C_2H_4 surface excess isotherms exhibit a maximum as a function of the pore diameter for the experimental studied temperatures. The micro- (<2 nm) and mesopore (2nm < d_{pore}< 50 nm) range is divided by a black dashed line.

Indeed, based on computational experiments [24,25], it is expected that above a critical pore size, the supercritical fluid does not show a pore size dependency concerning the reduced pressure corresponding to the surface excess maximum. To further evidence that this is indeed the case for C_2H_4 adsorption on CPG (18.5), the C_2H_4 surface excess isotherm on CPG (18.5) is compared with the adsorption of C_2H_4 on graphitized carbon black [21] at the same reduced temperature. Graphitized carbon black represents a nonporous carbon and hence the corresponding isotherms serves as a reference for adsorption of a supercritical fluid on a nonporous, planar surface. The surface excess isotherms are normalized to the specific surface area, illustrated in Figure 7, to allow a direct comparison. Both isotherms are in good agreement, suggesting that for the experimental condition studied, C_2H_4 adsorption in pores exceeding the lower PSD limit of 15 nm of CPG (18.5) can be considered as adsorption on a planar surface, i.e., the reduced pressure of the surface excess maximum does not depend on the pore size. The slightly higher surface excess amount of C_2H_4 observed on the graphitized carbon black can be explained by expected differences in the effective adsorption potential for C_2H_4 on graphitized carbon as compared to an amorphous silica surface. The comparison suggests that despite the fact that CPG is a mesoporous solids, under the given experimental conditions, there is no pore size/confinement effect observed and details of the effective solid-gas interactions have no effect on the position at which the surface excess isotherm exhibits a maximum, which is in agreement with theoretical lattice gas predictions [25].
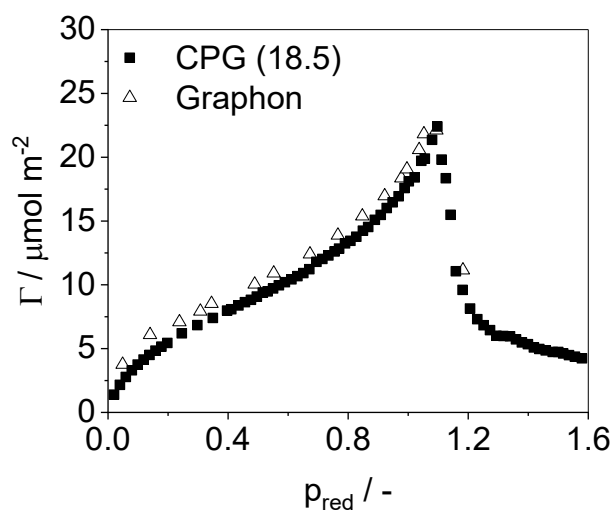
Figure 7: C_2H_4 surface excess isotherm normalized with regard to the specific surface area on CPG (18.5) and (non-porous) graphitized carbon black [21] at $T_{red} = 1.021$.

Hence, because confinement effects do not play a role, the strong increase of the surface excess concentration Γ when approaching the surface excess maximum is indicative of near-critical adsorption, i.e., multilayer adsorption caused by an increase of the correlation length of near-critical density fluctuations. In the vicinity of a non-critical solid, theoretical predictions [57,58] show that the dense adsorbate layer, i.e., at the pore wall, perturbates, depending on the correlation length, into the pore space. In a more simplified language, the term critical adsorption represents a not by the pore diameter limited far expansion of the multilayer adsorption into the pore space. In order to continue towards the investigation of whether a fluid-dependent pore-size effect occurs, in Figure 8 the surface excess isotherms of C_2H_4, CO_2 and

SF_6 under comparable experimental conditions are illustrated as a function of the reduced pressure on a) MCM-48 (3.3) and b) CPG (18.5). Starting again in the low pressure region, the adsorption of C_2H_4 and CO_2 is superimposed, indicating that both fluids might have a similar adsorption potential, while the data indicate that the effective fluid-wall interaction in the case of SF_6 is lower. This observation is supported by the isosteric heat of adsorption which is determined from the experimental data using the Clausius-Clapeyron approach [59] (see Supporting Information Figure S6-12), showing an identical course of the isosteric heat of adsorption in the low pressure region for CO_2 and C_2H_4, while the obtained heat for SF_6 is significantly lower. Figure 8a cleary indicates that for MCM-48 (3.3), which exhibits narrow mesopores with a mode pore diameter of 3.3 nm, the position of the surface excess maximum depends slightly on the choice of the fluid, whereas for the large pore CPG (18.5) the surface excess maximum of all the investigated fluids does not depend on pore size. The results in Figure 8 are in agreement with lattice gas predictions [25] obtained for slit pores.
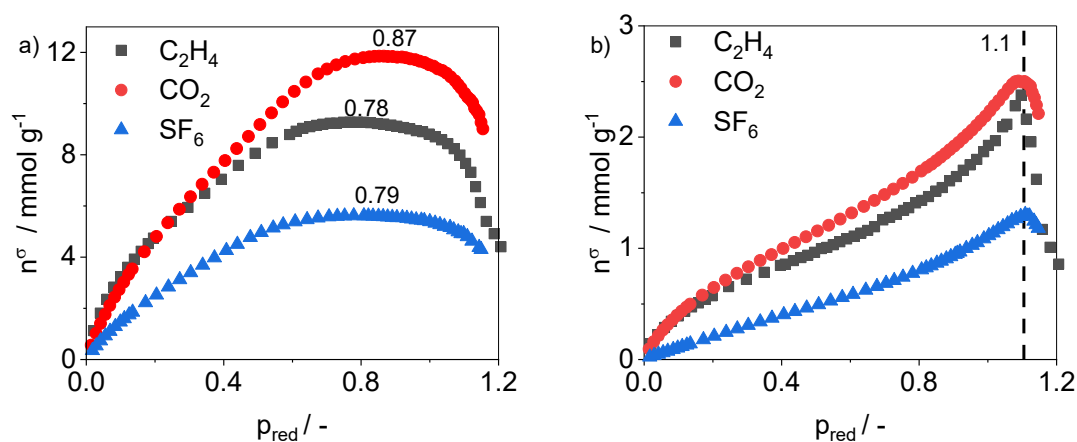
Figure 8: Surface excess isotherms of C_2H_4, CO_2 and SF_6 on a) MCM-48 (3.3) and b) CPG (18.5) at a reduced temperature of 1.021 and 1.023, respectively.

While the choice of highly ordered mesoporous molecular sieves allows us to investigate such subtle details, the investigation of a fluid dependent effect on the surface excess maximum is far less straightforward if quite disordered silica aerogel is used as adsorbent, exhibiting a wide pore size distribution, where the surface excess adsorption behavior of various gases were studied [31], contrary to our work.

In the following, we further investigate which factors are decisive for the pore size dependent effect on p^{max}, which is the pressure associated with the well-defined surface excess maximum observed in the mesoporous molecular sieves. Plotting the obtained reduced pressure of the maximum (for C_2H_4) as a function of the inverse pore-diameter (1/d), given in Figure 9a, the data suggest for C_2H_4 confined (at the given temperatures) in mesopores a linear-relationship. For the fluid adsorbed in the largest pores of CPG (18.5), the surface excess isotherms are not affected by confinement, i.e., no pore-size dependence of the surface excess maximum is observed, which is illustrated as a horizontal leveling off. With increasing temperature, this leveling off is shifted to higher reduced pressures.
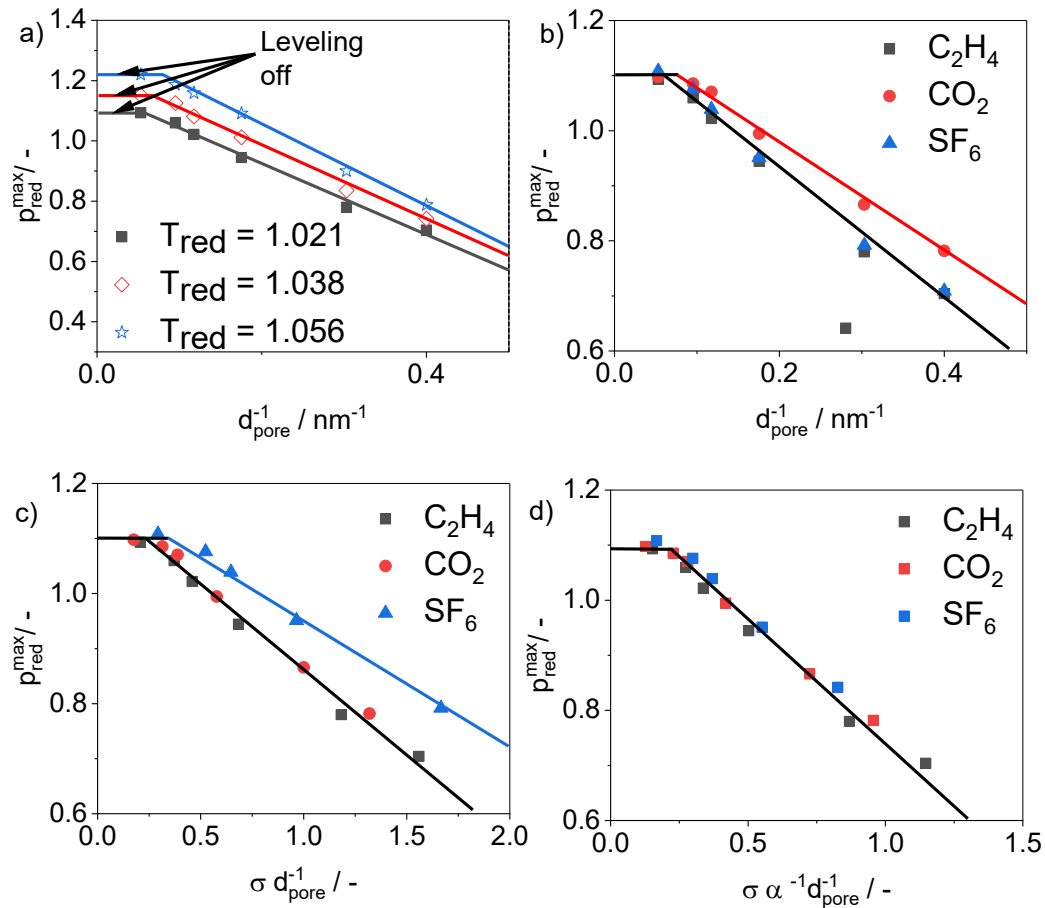
Figure 9: Reduced pressure where the surface excess isotherm exhibits its characteristic maximum for a) C_2H_4 adsorption on micro- and mesoporous materials at various temperatures as a function of the inverse pore diameter b) C_2H_4, CO_2 and SF_6 adsorption on mesoporous materials as a function of the inverse pore diameter c) C_2H_4, CO_2 and SF_6 adsorption on mesoporous materials as a function of the inverse pore diameter and the fluids' kinetic diameters d) C_2H_4, CO_2 and SF_6 adsorption on mesoporous materials as a function of the inverse pore diameter, the fluids' kinetic diameters and the microscopic wetting parameter.

Regarding the temperature dependence of p^{max}, the experimental data shows that with increasing temperature, the reduced pressure at which the surface excess isotherm exhibits a maximum is shifted to higher values, while the slope of the linear correlation slightly increases, following theoretical expectation. The surface excess maximum of NaY (1.1) shows severe deviations from the linear correlation observed in the mesopore region. Hence, the experimental findings suggest that the supercritical adsorption in micropores is distinct from the adsorption mechanism in mesopores. The isotherms of NaY (1.1), which reach their specific broad plateaus in the pressure range associated with the surface-dominated regime, emphasize this observation.

To compare the phenomenon for C_2H_4, CO_2 and SF_6, the reduced pressure of the surface excess maximum (for adsorption on mesoporous materials) for all three gases are shown as a function of the inverse pore diameter at $T_{red} = 1.021$ and 1.023, respectively, in Figure 9b. While the leveling off is fluid independent, the data show a superimposed linear correlation for C_2H_4 and SF_6, while the slope for CO_2 is smaller and the overall course is shifted to higher values.

Since any confined geometry effect will depend on the ratio of pore size to the kinetic molecular diameter, it is reasonable to reduce the pore diameter with regard to the kinetic diameter of the

fluid σ. Illustrating the results in Figure 9c, now C_2H_4 and CO_2 are in excellent agreement, while the slope of SF_6 is lower and shifted to higher values. Since our data suggest that C_2H_4 and CO_2 have relatively attractive fluid-wall interactions in the same order of magnitude, whereas SF_6 adsorption is well below, the experimental observations qualitatively follow the theoretical expectations of lattice gas predictions [25].

In order to derive a universal relationship, a metric for the relative strength of fluid-wall interactions must be incorporated into the simple relationship. Here, we use the so-called microscopic wetting parameter α_w [60–62]:

$$\alpha_w = \rho_s \sigma_{FS}^2 \Delta \frac{\epsilon_{FS}}{\epsilon_{FF}} \tag{2}$$

With the density of the adsorbent ρ_s, the structural parameter Δ, which is a measure of the distance between two consecutive planes of solid, σ_{FS} as a measure for the distance between the solid and the first adsorbate layer, the strength of the fluid-solid interactions ϵ_{FS} and the strength of the fluid-fluid interactions ϵ_{FF}. The parameters for the three gases and siliceous surfaces are taken from the literature [61,63] (see Supporting information Table S2 and S3). The solid-fluid potential parameters are obtained using the Lorenz-Berthelot combinatorial rule, leading to an effective adsorptive-adsorbent interaction parameter, i.e., the above mention parameter α_w, of 1.36 for C_2H_4, 1.38 for CO_2 and 1.75 for SF_6. The obtained parameters are in agreement with our experimental observations that C_2H_4 and CO_2 have a similar adsorption potential on siliceous surfaces while SF_6 is much more weakly adsorbed. Introducing the inverse interaction parameter $1/\alpha_w$ as prefactor, the experimental data, which is illustrated in Figure 9 d), suggests a universal relationship between the reduced pressure at which a fluid confined in a cylindrical mesopore exhibits a maximum and the pore size, the kinetic diameter of the fluid and the effective adsorptive/adsorbent interaction parameter α_w:

$$p_{red}^{conf,max} \propto \frac{\sigma}{\alpha_w \, d_{pore}} \tag{3}$$

In the following, the temperature dependence of the phenomenon (observed in mesopores) is further investigated. Therefore, two cases have to be distinguished: the essentially unconfined (i.e., as demonstrated for the 18.5 nm of the CPG material) and the mesoporous molecular sieves, where a pore size dependent confinement effect on the surface excess maximum has been observed. For the adsorption of an unconfined fluid, our data on silica and adsorption data on graphitized carbon black taken from the literature [21], illustrated in Figure 10 a), suggest a linear relationship with $\left((T - T_c) T_c^{-1} \right)^v$, obeying the same temperature dependence as the maximum of the compressibility of bulk C_2H_4 (see Supporting Information Figure S5 & S13). For the case of a fluid confined in a cylindrical mesopore, by extracting the slope of the linear relationship from Figure 9d (compare Supporting Information Figure S14 and for $T_{red} = 1.038$ and 1.056 Figure S15 and S16), we find that the temperature dependence of the slope can be modeled (for the experimental conditions investigated) following a power law $\Big((T -$

$\mathbf{T_c)T_c^{-1}}\Big)^{-\nu}$, which is illustrated in Figure 10 b) and is identical to the temperature dependence of the correlation length.
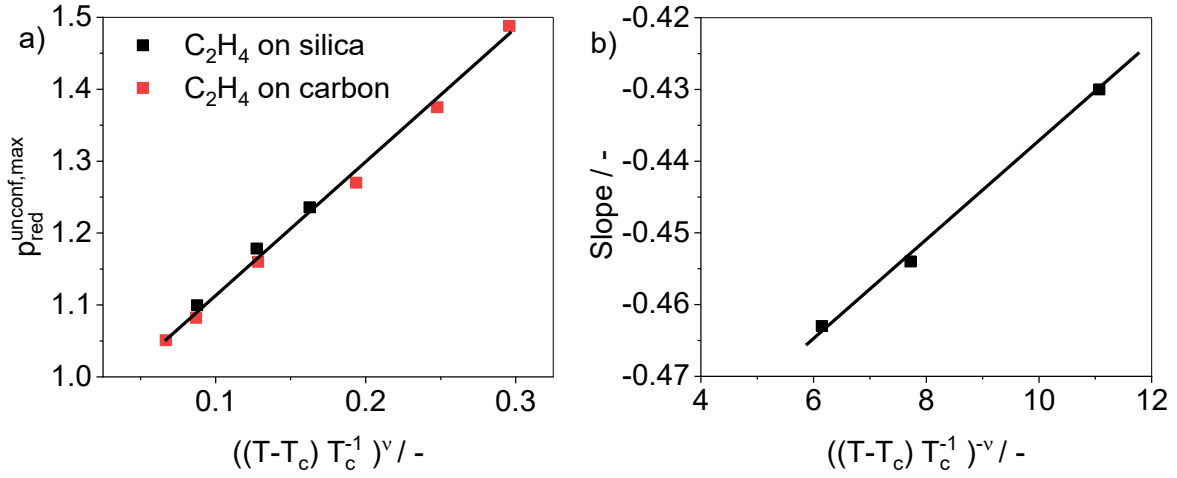
Figure 10: Temperature dependence of a) the reduced pressure where the surface excess isotherm of an unconfined fluid on silica (CPG (18.5)) and nonporous carbon black[21] exhibits a maximum b) the slope of the linear-relationship between the maximum, pore-size, kinetic diameter and microscopic wetting parameter.

Our data suggest that with decreasing pore size and increased confinement effect the surface excess maximum shift to smaller reduced pressure for a give supercritical temperature while the surface excess maximum changes from a distinct cusp-like form to a much more rounded, far less pronounced surface excess maximum for smaller pore sizes. This behavior is in line with a suppression (near the critical point) of density fluctuations (i.e., the correlation length of the density fluctuations cannot increase the pore dimensions) coupled with a corresponding decrease of isothermal compressibility.

For the same reason it is known that this suppression of critical point fluctuations in pores leads to a shift of the critical temperature to lower values [47,64]. Using scaling theory of large pores the critical temperature shift should obey the following relation [65,66]:

$$\frac{T-T_c}{T_c} \propto d_{Pore}^{-\frac{1}{\nu}} \qquad (4)$$

with the critical exponent $\nu = 0.64$. However, for more narrow mesopores, as studied in this paper, it is predicted that the shift of the critical temperature should be linearly dependent with the inverse pore diameter d_{Pore}^{-1} and the kinetic diameter σ of the fluid [67]:

$$\frac{T-T_c}{T} \propto \frac{\sigma}{d_{Pore}} \qquad (5)$$

This relationship for the critical temperature shift is remarkably similar to our observed unique relationship between the pore size and position of the surface excess maximum for mesopores. Hence this indicates indeed that in both cases there is a common cause for the observed behavior, i.e., the effect of confinement on state of the pore fluid, which is a suppression of the

correlations length of density fluctuations and the effect on the state of the pore fluid (which at given temperatures differs the more from the bulk fluid the more narrow the pore is).

4 Conclusion

To address open fundamental questions of how pore structure and the resulting confinement affects the supercritical adsorption behavior of pure fluids , we have performed a fundamental experimental study assessing the effect of pore size on the supercritical adsorption behaviour of pure fluids such as C_2H_4, CO_2 and SF_6 over a wide range of temperatures (from $T/Tc = 1.021$ to $T/Tc = 1.06$) and pressures up to 95 bar)) on a series of model materials exhibiting well defined pore sizes with narrow pore size distributions, i.e., ordered micro- and mesoporous materials such as zeolites, mesoporous silica molecular sieves (e.g., KIT-6, MCM-48) but also in controlled pore glass (CPG). The obtained set of unique experimental data clearly demonstrates how the shape of the surface excess isotherm is affected by the interplay between the states of the pore and bulk fluid (i.e., in particular with regard to the effective fluid compressibility, depending on the proximity to the bulk critical point). Based on our data, we suggest that the surface excess isotherms of a given adsorptive can be divided into three pressure regimes: at lower pressures, the surface excess amount depends for the silica materials studied here solely on the underlying specific surface area, whereas at higher pressure the increase and shape of the surface excess isotherm is affected by both the state of the pore- and core fluid. The observed decrease of the surface excess amount at high pressures, exceeding the surface excess maximum, can be mainly attributed to the properties of the bulk fluid.

Most importantly, our systematic experiments suggests for a given temperature a novel and unique correlation between the pressure of the surface excess maximum p^{max} and the mesopore size taking into account the kinetic diameter of the fluid and the attractive fluid-wall interaction for a given adsorptive/adsorbent system (e.g.,SF_6/silica and CO_2/silica). However, for the experimental temperatures investigated, no pore size effect on the surface excess maximum can be observed for pores with a mode pore diameter larger than ca. 15 nm. Going more into detail, for the controlled pore glass, we could demonstrate that the shape of the obtained surface excess isotherm is identical with surface excess adsorption on a nonporous carbon surface, i.e., the position of the surface excess maximum depends mainly on the state of the bulk fluid and its effective isothermal compressibility (which depends on the distance to the bulk critical point). For smaller pores confinement effects on the state of the pore fluid become important, leading to the observed pore size effect on the surface excess maximum.

Summarizing, the insights gained in this work contribute to a better understanding of the underlying adsorption mechanism of supercritical fluids in nanoporous materials. Our results suggest important structure-property relationships allowing one to determine, for given thermodynamic conditions, important information for optimizing operational conditions in supercritical adsorption applications and may also contribute to the development of optimized adsorbent materials tailored towards gas storage and separation applications.

To gain an even deeper understanding of the mechanisms that are dominating the surface excess isotherms of supercritical fluids confined in nanoporous materials, ongoing work is expanding

our investigation mainly into the microporous range (utilising zeolites and MOFs) including additional adsorptives such as hydrogen and methane coupled with complementary molecular simulations.

Supporting Information

Surface excess and (absolute) adsorbed amount isotherms on various materials; validation of the experimental setup; C_2H_4 surface excess data on various materials at $T_{red} = 1.038$ and $T_{red} = 1.056$; compressibility of bulk C_2H_4; determination of the isochoric heat of adsorption for C_2H_4, CO_2 and SF_6; structural and adsorptive/adsorbents (interaction) parameters for the determination of the microscopic wetting parameter; temperature dependence of p_{max} for both the case of an unconfined and (in a mesopores) confined fluid

Acknowledgement

References

(1)   Langmi, H. W.; Ren, J.; North, B.; Mathe, M.; Bessarabov, D. Hydrogen Storage in Metal-Organic Frameworks: A Review. *Electrochimica Acta* **2014**, *128*, 368–392. https://doi.org/10.1016/j.electacta.2013.10.190.
(2)   Hirscher, M.; Panella, B. Hydrogen Storage in Metal–Organic Frameworks. *Scr. Mater.* **2007**, *56* (10), 809–812. https://doi.org/10.1016/j.scriptamat.2007.01.005.
(3)   Zhao, D.; Yuan, D.; Zhou, H.-C. The Current Status of Hydrogen Storage in Metal–Organic Frameworks. *Energy Environ. Sci.* **2008**, *1* (2), 222–235. https://doi.org/10.1039/B808322N.
(4)   Frolich, P. K.; White, A. Adsorption of Methane and Hydrogen on Charcoal at High Pressure. *Ind. Eng. Chem.* **1930**, *22*. https://doi.org/10.1021/ie50250a014.
(5)   von Antropoff, A. Untersuchungen über die Adsorption von Gasen von kleinsten bis zu höchsten Drucken. *Kolloid-Z.* **1952**, *129*. https://doi.org/10.1007/BF01802754.
(6)   Lowell, S.; Shields, J. E.; Thomas, M. A.; Thommes, M. *Characterization of Porous Solids and Powders: Surface Area, Pore Size and Density*, 1st ed.; Springer-Verlag, 2004.
(7)   Gibbs, J. W. *The Collected Works*; New Haven; Vol. 1.
(8)   Gumma, S.; Talu, O. Net Adsorption: A Thermodynamic Framework for Supercritical Gas Adsorption and Storage in Porous Solids. *Langmuir* **2010**, *26*. https://doi.org/10.1021/la102186q.
(9)   Brandani, S.; Mangano, E.; Sarkisov, L. Net, Excess and Absolute Adsorption and Adsorption of Helium. *Adsorption* **2016**, *22* (2), 261–276. https://doi.org/10.1007/s10450-016-9766-0.
(10)   Myers, A. L.; Monson, P. A. Physical Adsorption of Gases: The Case for Absolute Adsorption as the Basis for Thermodynamic Analysis. *Adsorption* **2014**, *20* (4), 591–622. https://doi.org/10.1007/s10450-014-9604-1.

(11) Murata, K.; El-Merraoui, M.; Kaneko, K. A New Determination Method of Absolute Adsorption Isotherm of Supercritical Gases under High Pressure with a Special Relevance to Density-Functional Theory Study. *J. Chem. Phys.* **2001**, *114*. https://doi.org/10.1063/1.1344926.

(12) Moellmer, J.; Celer, E. B.; Luebke, R.; Cairns, A. J.; Staudt, R.; Eddaoudi, M.; Thommes, M. Insights on Adsorption Characterization of Metal-Organic Frameworks: A Benchmark Study on the Novel Soc-MOF. *Microporous Mesoporous Mater.* **2010**, *129*. https://doi.org/10.1016/j.micromeso.2009.06.014.

(13) Salem, M. M. K.; Braeuer, P.; Szombathely, M. v.; Heuchel, M.; Harting, P.; Quitzsch, K.; Jaroniec, M. Thermodynamics of High-Pressure Adsorption of Argon, Nitrogen, and Methane on Microporous Adsorbents. *Langmuir* **1998**, *14*. https://doi.org/10.1021/la970119u.

(14) Pini, R.; Ottiger, S.; Rajendran, A.; Storti, G.; Mazzotti, M. Reliable Measurement of Near-Critical Adsorption by Gravimetric Method. *Adsorption* **2006**, *12*. https://doi.org/10.1007/s10450-006-0567-8.

(15) Nguyen, H. G. T.; Sims, C. M.; Toman, B.; Horn, J.; van Zee, R. D.; Thommes, M.; Ahmad, R.; Denayer, J. F. M.; Baron, G. V.; Napolitano, E.; Bielewski, M.; Mangano, E.; Brandani, S.; Broom, D. P.; Benham, M. J.; Dailly, A.; Dreisbach, F.; Edubilli, S.; Gumma, S.; Möllmer, J.; Lange, M.; Tian, M.; Mays, T. J.; Shigeoka, T.; Yamakita, S.; Hakuman, M.; Nakada, Y.; Nakai, K.; Hwang, J.; Pini, R.; Jiang, H.; Ebner, A. D.; Nicholson, M. A.; Ritter, J. A.; Farrando-Pérez, J.; Cuadrado-Collados, C.; Silvestre-Albero, J.; Tampaxis, C.; Steriotis, T.; Řimnáčová, D.; Švábová, M.; Vorokhta, M.; Wang, H.; Bovens, E.; Heymans, N.; De Weireld, G. A Reference High-Pressure CH4 Adsorption Isotherm for Zeolite Y: Results of an Interlaboratory Study. *Adsorption* **2020**, *26* (8), 1253–1266. https://doi.org/10.1007/s10450-020-00253-0.

(16) Nguyen, H. G. T.; Espinal, L.; van Zee, R. D.; Thommes, M.; Toman, B.; Hudson, M. S. L.; Mangano, E.; Brandani, S.; Broom, D. P.; Benham, M. J.; Cychosz, K.; Bertier, P.; Yang, F.; Krooss, B. M.; Siegelman, R. L.; Hakuman, M.; Nakai, K.; Ebner, A. D.; Erden, L.; Ritter, J. A.; Moran, A.; Talu, O.; Huang, Y.; Walton, K. S.; Billemont, P.; De Weireld, G. A Reference High-Pressure CO2 Adsorption Isotherm for Ammonium ZSM-5 Zeolite: Results of an Interlaboratory Study. *Adsorption* **2018**, *24* (6), 531–539. https://doi.org/10.1007/s10450-018-9958-x.

(17) Hurst, K. E.; Gennett, T.; Adams, J.; Allendorf, M. D.; Balderas-Xicohténcatl, R.; Bielewski, M.; Edwards, B.; Espinal, L.; Fultz, B.; Hirscher, M. An International Laboratory Comparison Study of Volumetric and Gravimetric Hydrogen Adsorption Measurements. *ChemPhysChem* **2019**, *20* (15), 1997–2009.

(18) Moretto, P.; Zlotea, C.; Dolci, F.; Amieiro, A.; Bobet, J.-L.; Borgschulte, A.; Chandra, D.; Enoki, H.; De Rango, P.; Fruchart, D.; Jepsen, J.; Latroche, M.; Jansa, I. L.; Moser, D.; Sartori, S.; Wang, S. M.; Zan, J. A. A Round Robin Test Exercise on Hydrogen Absorption/Desorption Properties of a Magnesium Hydride Based Material. *Int. J. Hydrog. Energy* **2013**. https://doi.org/10.1016/j.ijhydene.2013.03.118.

(19) Zlotea, C.; Moretto, P.; Steriotis, T. A Round Robin Characterisation of the Hydrogen Sorption Properties of a Carbon Based Material. *Int. J. Hydrog. Energy* **2009**, *34*. https://doi.org/10.1016/j.ijhydene.2009.01.079.

(20) Wu, T.; Zhao, H.; Tesson, S.; Firoozabadi, A. Absolute Adsorption of Light Hydrocarbons and Carbon Dioxide in Shale Rock and Isolated Kerogen. *Fuel* **2019**, *235*, 855–867. https://doi.org/10.1016/j.fuel.2018.08.023.

(21) Specovius, J.; Findenegg, G. H. Study of a Fluid/Solid Interface over a Wide Density Range Including the Critical Region. I. Surface Excess of Ethylene/Graphite. *Berichte Bunsenges. Für Phys. Chem.* **1980**, *84* (7). https://doi.org/10.1002/bbpc.19800840715.

(22) Physical Adsorption: Experiment, Theory and Applications; Fraissard, J., Ed.; Springer Netherlands: Dordrecht, 1997. https://doi.org/10.1007/978-94-011-5672-1.

(23) van Megen, W.; Snook, I. K. Physical Adsorption of Gases at High Pressure. *Mol. Phys.* **1985**, *54* (3), 741–755. https://doi.org/10.1080/00268978500100591.

(24) Tan, Ziming.; Gubbins, K. E. Adsorption in Carbon Micropores at Supercritical Temperatures. *J. Phys. Chem.* **1990**, *94* (15), 6061–6069. https://doi.org/10.1021/j100378a079.

(25) Hocker, T.; Rajendran, A.; Mazzotti, M. Measuring and Modeling Supercritical Adsorption in Porous Solids. Carbon Dioxide on 13X Zeolite and on Silica Gel. *Langmuir* **2003**, *19* (4), 1254–1267. https://doi.org/10.1021/la0266379.

(26) Pini, R.; Ansari, H.; Hwang, J. Measurement and Interpretation of Unary Supercritical Gas Adsorption Isotherms in Micro-Mesoporous Solids. *Adsorption* **2021**, *27* (4), 659–671. https://doi.org/10.1007/s10450-021-00313-z.

(27) Humayun, R.; Tomasko, D. L. High-Resolution Adsorption Isotherms of Supercritical Carbon Dioxide on Activated Carbon. *AIChE J.* **2000**, *46* (10), 2065–2075. https://doi.org/10.1002/aic.690461017.

(28) Rother, G.; Vlcek, L.; Gruszkiewicz, M. S.; Chialvo, A. A.; Anovitz, L. M.; Bañuelos, J. L.; Wallacher, D.; Grimm, N.; Cole, D. R. Sorption Phase of Supercritical CO2 in Silica Aerogel: Experiments and Mesoscale Computer Simulations. *J. Phys. Chem. C* **2014**, *118* (28), 15525–15533. https://doi.org/10.1021/jp503739x.

(29) Pini, R.; Ottiger, S.; Rajendran, A.; Storti, G.; Mazzotti, M. Near-Critical Adsorption of CO2 on 13X Zeolite and N 2 O on Silica Gel: Lack of Evidence of Critical Phenomena. *Adsorption* **2008**, *14* (1), 133–141. https://doi.org/10.1007/s10450-007-9080-y.

(30) Rother, G.; Krukowski, E. G.; Wallacher, D.; Grimm, N.; Bodnar, R. J.; Cole, D. R. Pore Size Effects on the Sorption of Supercritical CO2 in Mesoporous CPG-10 Silica. *J. Phys. Chem. C* **2012**, *116* (1), 917–922. https://doi.org/10.1021/jp209341q.

(31) Gruszkiewicz, M. S.; Rother, G.; Vlček, L.; DiStefano, V. H. Supercritical Fluid Adsorption to Weakly Attractive Solids: Universal Scaling Laws. *J. Phys. Chem. C* **2018**, *122* (27), 15558–15566. https://doi.org/10.1021/acs.jpcc.8b04390.

(32) Chahine, R.; Bose, T. K. Characterization and Optimization of Adsorbents for Hydrogen Storage., 1996.

(33) Bastos-Neto, M.; Patzschke, C.; Lange, M.; Möllmer, J.; Möller, A.; Fichtner, S.; Schrage, C.; Lässig, D.; Lincke, J.; Staudt, R.; Krautscheid, H.; Gläser, R. Assessment of Hydrogen Storage by Physisorption in Porous Materials. *Energy Environ. Sci.* **2012**, *5*. https://doi.org/10.1039/C2EE22037G.

(34) Dai, Z.; Middleton, R.; Viswanathan, H.; Fessenden-Rahn, J.; Bauman, J.; Pawar, R.; Lee, S.-Y.; McPherson, B. An Integrated Framework for Optimizing CO2 Sequestration and Enhanced Oil Recovery. *Environ. Sci. Technol. Lett.* **2014**, *1*. https://doi.org/10.1021/ez4001033.

(35) Firoozabadi, A.; Myint, P. C. Prospects for Subsurface CO 2 Sequestration. *AIChE J.* **2010**, *56*. https://doi.org/10.1002/aic.12287.

(36) Yamasaki, A. An Overview of CO2 Mitigation Options for Global Warming—Emphasizing CO2 Sequestration Options. *J. Chem. Eng. Jpn.* **2003**, *36*. https://doi.org/10.1252/jcej.36.361.

(37) Bains, P.; Psarras, P.; Wilcox, J. CO2 Capture from the Industry Sector. *Prog. Energy Combust. Sci.* **2017**, *63*. https://doi.org/10.1016/j.pecs.2017.07.001.

(38) Barker, D. J.; Turner, S. A.; Napier-Moore, P. A.; Clark, M.; Davison, J. E. CO2 Capture in the Cement Industry. *Energy Procedia* **2009**, *1*. https://doi.org/10.1016/j.egypro.2009.01.014.

(39) Kleitz, F.; Choi, S. H.; Ryoo, R. Cubic Ia3d Large Mesoporous Silica: Synthesis and Replication to Platinum Nanowires, Carbon Nanorods and Carbon Nanotubes. *Chem. Commun.* **2003**, *17*. https://doi.org/10.1039/B306504A.

(40) Kleitz, F.; Bérubé, F.; Guillet-Nicolas, R.; Yang, C.-M.; Thommes, M. Probing Adsorption, Pore Condensation, and Hysteresis Behavior of Pure Fluids in Three-Dimensional Cubic Mesoporous KIT-6 Silica. *J. Phys. Chem. C* **2010**, *114* (20), 9344–9355. https://doi.org/10.1021/jp909836v.

(41) Kim, T.-W.; Chung, P.-W.; Lin, V. S.-Y. Facile Synthesis of Monodisperse Spherical MCM-48 Mesoporous Silica Nanoparticles with Controlled Particle Size. *Chem. Mater.* **2010**, *22*. https://doi.org/10.1021/cm1017344.

(42) Kleitz, F.; Schmidt, W.; Schüth, F. Calcination Behavior of Different Surfactant-Templated Mesostructured Silica Materials. *Microporous Mesoporous Mater.* **2003**, *65* (1), 1–29. https://doi.org/10.1016/S1387-1811(03)00506-7.

(43) Anunziata, O. A.; Beltramone, A. R.; Martínez, M. L.; Belon, L. L. Synthesis and Characterization of SBA-3, SBA-15, and SBA-1 Nanostructured Catalytic Materials. *J. Colloid Interface Sci.* **2007**, *315* (1), 184–190. https://doi.org/10.1016/j.jcis.2007.06.033.

(44) Thommes, M.; Kaneko, K.; Neimark, A. V.; Olivier, J. P.; Rodriguez-Reinoso, F.; Rouquerol, J.; Sing, K. S. W. Physisorption of Gases, with Special Reference to the Evaluation of Surface Area and Pore Size Distribution (IUPAC Technical Report). *Pure Appl. Chem.* **2015**, *87* (9–10), 1051–1069. https://doi.org/10.1515/pac-2014-1117.

(45) Dreisbach, F.; Lösch, H. W. Magnetic Suspension Balance For Simultaneous Measurement of a Sample and the Density of the Measuring Fluid. **2000**, 7.

(46) Nguyen, H. G. T.; Horn, J. C.; Thommes, M.; Zee, R. D. van; Espinal, L. Experimental Aspects of Buoyancy Correction in Measuring Reliable High-Pressure Excess Adsorption Isotherms Using the Gravimetric Method. *Meas. Sci. Technol.* **2017**, *28* (12), 125802. https://doi.org/10.1088/1361-6501/aa8f83.

(47) Gelb, L. D.; Gubbins, K. E.; Radhakrishnan, R.; Sliwinska-Bartkowiak, M. Phase Separation in Confined Systems. *Rep. Prog. Phys.* **1999**, *62* (12), 1573–1659. https://doi.org/10.1088/0034-4885/62/12/201.

(48) Schlumberger, C.; Thommes, M. Characterization of Hierarchically Ordered Porous Materials by Physisorption and Mercury Porosimetry—A Tutorial Review. *Adv. Mater. Interfaces* **2021**, *8* (4), 2002181. https://doi.org/10.1002/admi.202002181.

(49) Klinowski, J.; Ramdas, S.; M. Thomas, J.; A. Fyfe, C.; Steven Hartman, J. A Re-Examination of Si, Al Ordering in Zeolites NaX and NaY. *J. Chem. Soc. Faraday Trans. 2 Mol. Chem. Phys.* **1982**, *78* (7), 1025–1050. https://doi.org/10.1039/F29827801025.

(50) Thommes, M.; Smarsly, B.; Groenewolt, M.; Ravikovitch, P. I.; Neimark, A. V. Adsorption Hysteresis of Nitrogen and Argon in Pore Networks and Characterization of Novel Micro- and Mesoporous Silicas. *Langmuir* **2006**, *22* (2), 756–764. https://doi.org/10.1021/la051686h.

(51) Schlumberger, C.; Sandner, L.; Michalowski, A.; Thommes, M. Reliable Surface Area Assessment of Wet and Dry Nonporous and Nanoporous Particles: Nuclear Magnetic Resonance Relaxometry and Gas Physisorption. *Langmuir* **2023**, *39* (13), 4611–4621. https://doi.org/10.1021/acs.langmuir.2c03337.

(52) Cychosz, K. A.; Guillet-Nicolas, R.; García-Martínez, J.; Thommes, M. Recent Advances in the Textural Characterization of Hierarchically Structured Nanoporous Materials. *Chem. Soc. Rev.* **2017**, *46* (2), 389–414. https://doi.org/10.1039/C6CS00391E.

(53) Schlumberger, C.; Scherdel, C.; Kriesten, M.; Leicht, P.; Keilbach, A.; Ehmann, H.; Kotnik, P.; Reichenauer, G.; Thommes, M. Reliable Surface Area Determination of Powders and Meso/Macroporous Materials: Small-Angle X-Ray Scattering and Gas Physisorption. *Microporous Mesoporous Mater.* **2022**, *329*, 111554. https://doi.org/10.1016/j.micromeso.2021.111554.

(54) Rouquerol, J.; Llewellyn, P.; Rouquerol, F. Is the Bet Equation Applicable to Microporous Adsorbents? In *Studies in Surface Science and Catalysis*; Llewellyn, P. L., Rodriquez-Reinoso, F., Rouqerol, J., Seaton, N., Eds.; Characterization of Porous Solids VII; Elsevier, 2007; Vol. 160, pp 49–56. https://doi.org/10.1016/S0167-2991(07)80008-5.

(55) Sotomayor, F.; Cychosz, K.; Thommes, M. Characterization of Micro/Mesoporous Materials by Physisorption: Concepts and Case Studies. Acc. Mater. Surf. Res. **2018, Vol. 3, pp 34-50**.

(56) Di Giovanni, O.; Dörfler, W.; Mazzotti, M.; Morbidelli, M. Adsorption of Supercritical Carbon Dioxide on Silica. *Langmuir* **2001**, *17* (14), 4316–4321. https://doi.org/10.1021/la010061q.

(57) Kuz'min, V. L.; Kuni, F. M.; Rusanov, A. I. *Russ. J. Phys. Chem.* **1972**, *46*.

(58) Widom, B. Noncritical Interface near a Critical End Point. *J. Chem. Phys.* **1977**, *67*.

(59) Gmehling, J.; Kleiber, M.; Kolbe, B.; Rarey, J. *Chemical Thermodynamics for Process Simulation*; John Wiley & Sons, 2019.

(60) Gubbins, K. E.; Long, Y.; Śliwinska-Bartkowiak, M. Thermodynamics of Confined Nano-Phases. *J. Chem. Thermodyn.* **2014**, *74*. https://doi.org/10.1016/j.jct.2014.01.024.

(61) Radhakrishnan, R.; Gubbins, K. E.; Sliwinska-Bartkowiak, M. Global Phase Diagrams for Freezing in Porous Media. *J. Chem. Phys.* **2002**, *116*. https://doi.org/10.1063/1.1426412.

(62) Śliwińska-Bartkowiak, M.; Sterczyńska, A.; Long, Y.; Gubbins, K. E. Influence of Microroughness on the Wetting Properties of Nano-Porous Silica Matrices. *Mol. Phys.* **2014**, *112*. https://doi.org/10.1080/00268976.2014.935820.

(63) Hirschfelder, J. O.; Curtiss, C. F.; Bird, R. B. *Molecular Theory of Gases and Liquids*, 1st ed.; Wiley-Interscience, 1966.

(64) Thommes, M.; Findenegg, G. H. Pore Condensation and Critical-Point Shift of a Fluid in Controlled-Pore Glass. *Langmuir* **1994**, *10* (11), 4270–4277. https://doi.org/10.1021/la00023a058.

(65) Fisher, M. E.; Nakanishi, H. Scaling Theory for the Criticality of Fluids between Plates. *J. Chem. Phys.* **1981**, *75*. https://doi.org/10.1063/1.442035.

(66) Nakanishi, H.; Fisher, M. E. Critical Point Shifts in Films. *J. Chem. Phys.* **1983**, *78*. https://doi.org/10.1063/1.445087.

(67) Evans, R.; Bettolo Marconi, U. M.; Tarazona, P. Capillary Condensation and Adsorption in Cylindrical and Slit-like Pores. *J. Chem. Soc. Faraday Trans. 2 Mol. Chem. Phys.* **1986**, *82*. https://doi.org/10.1039/F29868201763.

TOC Graphic

Nanoporous Materials

Supercritical
Adsorption Behavior

Gas Storage
Applications

Γ

1 nm d_{Pore} 20 nm

3.3   8.5

1.1

18.5

p   80 bar

p^{max}

CO_2

C_2H_4

SF_6

c d^{-1}_{Pore}